AGU PUBLICATIONS

JGR

Journal of Geophysical Research: Planets

RESEARCH ARTICLE
10.1002/2016JE005037

Key Points:
- We estimated Mercury's gravity field, tidal Love number, and spin state based on more than 3 years of MESSENGER radio tracking data
- Our estimate of the Love number indicates that Mercury's mantle may be hotter and weaker than previously thought
- Our estimate of the spin state parameters indicates that the gravity field and crust rotate about nearly the same axis

Correspondence to:
A. K. Verma,
ashokverma@ucla.edu

Citation:
Verma, A. K. and J.-L. Margot (2016), Mercury's gravity, tides, and spin from MESSENGER radio science data, *J. Geophys. Res. Planets*, *121*, doi:10.1002/2016JE005037.

Received 19 MAR 2016
Accepted 3 AUG 2016
Accepted article online 8 AUG 2016

Mercury's gravity, tides, and spin from MESSENGER radio science data

Ashok Kumar Verma[1] and Jean-Luc Margot[1,2]

[1]Department of Earth, Planetary, and Space Sciences, University of California, Los Angeles, California, USA, [2]Department of Physics and Astronomy, University of California, Los Angeles, California, USA

Abstract We analyze radio tracking data obtained during 1311 orbits of the MErcury Surface, Space ENvironment, GEochemistry, and Ranging (MESSENGER) spacecraft in the period March 2011 to April 2014. A least squares minimization of the residuals between observed and computed values of two-way range and Doppler allows us to solve for a model describing Mercury's gravity, tidal response, and spin state. We use a spherical harmonic representation of the gravity field to degree and order 40 and report error bars corresponding to 10 times the formal uncertainties of the fit. Our estimate of the product of Mercury's mass and the gravitational constant, $GM = (22031.87404 \pm 9 \times 10^{-4})$ km^3 s^{-2}, is in excellent agreement with published results. Our solution for the geophysically important second-degree coefficients ($\bar{C}_{2,0} = -2.25100 \times 10^{-5} \pm 1.3 \times 10^{-9}$, $\bar{C}_{2,2} = 1.24973 \times 10^{-5} \pm 1.2 \times 10^{-9}$) confirms previous estimates to better than 0.4% and, therefore, inferences about Mercury's moment of inertia and interior structure. Our estimate of the tidal Love number $k_2 = 0.464 \pm 0.023$ indicates that Mercury's mantle may be hotter and weaker than previously thought. Our spin state solution suggests that gravity-based estimates of Mercury's spin axis orientation are marginally consistent with previous measurements of the orientation of the crust.

1. Introduction

The MErcury Surface, Space ENvironment, GEochemistry, and Ranging (MESSENGER) mission [*Solomon et al.*, 2001] returned a wealth of data about the innermost planet in the solar system. The mission included a radio science investigation [*Srinivasan et al.*, 2007] that provided a key capability for characterizing Mercury's interior structure [e.g., *Smith et al.*, 2012; *Mazarico et al.*, 2014]. Here we analyzed over 3 years of radio tracking data with software and strategies that are different from those used in previous investigations.

Our motivations for this investigation are fourfold: (1) The k_2 tidal Love number provides powerful constraints on interior models of Mercury. An existing determination ($k_2 = 0.451 \pm 0.014$ [*Mazarico et al.*, 2014]) favors a cold (basal temperature of 1600 K) and stiff (rigidity of 71 GPa) mantle with no FeS layer [*Padovan et al.*, 2014]. However, *Mazarico et al.* [2014] indicate that they cannot rule out a wider range of values ($k_2 = 0.43 - 0.50$) which admit a greater variety of plausible interior models [*Padovan et al.*, 2014]. We are seeking an independent estimate of k_2 and its uncertainties to further constrain interior models. (2) *Mazarico et al.* [2014] provided a solution for Mercury's spin axis orientation that differs from the Earth-based radar solution [*Margot et al.*, 2012]. This may indicate an error in either or both determinations or a real difference between the orientations about which the gravity field and the crust rotate. *Peale et al.* [2016] have shown that the core spin axis may be misaligned from the mantle spin axis, and such a difference, if present, may be detectable. An independent determination of the spin axis orientation based on gravity data is needed to make progress on this issue. (3) If the misalignment between core and mantle spin axes is sufficiently large, the determination of the moment of inertia of the planet based on spin and gravity data [*Margot et al.*, 2012] may be jeopardized [*Peale et al.*, 2016]. In that case, the k_2 tidal Love number will play an even more important role in determining the interior structure of Mercury, and it warrants an independent determination. (4) Preflight simulations indicated that recovery of the longitudinal librations should be achievable at the 8% level from analysis of topography and gravity data [*Zuber and Smith*, 1997]. Although measurements of the librations have been obtained from Earth-based radar [*Margot et al.*, 2012] and from comparison of digital elevation models (DEMs) and laser altimetry data [*Stark et al.*, 2015], no gravity-based estimates currently exist. Here we describe how a gravity solution could be used to quantify the libration signal.

Table 1. Antenna Offsets[a] in the Spacecraft Frame With Origin at the Adapter Ring[b]

Antenna	Type	*X* (m)	*Y* (m)	*Z* (m)
Front LGA	low gain	−0.1270	−1.0348	−1.9939
Back LGA	low gain	0.1095	1.2753	−1.4262
AFT LGA	low gain	−0.2794	−0.8593	0.3686
FWD LGA	low gain	0.2794	−0.8593	−2.2291
Front FBA	medium gain	−0.7272	−0.6487	−1.6162
Back FBA	medium gain	0.2743	1.1394	−1.2603
Front PAA	high gain	−0.7272	−0.6487	−1.6162
Back PAA	high gain	0.2743	1.1394	−1.2603

[a]MESSENGER center of mass is offset by 0.89662 m from the adapter ring along the *Z* direction [*Planetary Data System*, 2016b].
[b]LGA: low-gain antenna, FBA: fanbeam antenna, PAA: phased-array antenna.

Our efforts are driven by the fact that knowledge of the spin axis orientation, Love number, and longitudinal librations are all essential for a determination of Mercury's interior structure [e.g., *Hauck et al.*, 2013].

2. Spacecraft Data

Radio tracking of the MESSENGER spacecraft resulted in several sets of observables, including one-way Doppler, two-way Doppler, and two-way range.

These products are available on the Planetary Data System (PDS) [*Planetary Data System*, 2016a], and documentation is provided by *Perry* [2011]. The typical precision of the two-way Doppler measurements (X band, uplink at 7.2 GHz, downlink at 8.4 GHz) as measured during the first 400 days of cruise was 0.03 mm/s with an integration time of 60 s [*Srinivasan et al.*, 2007]. *Mazarico et al.* [2014] showed that in-orbit residuals were almost always less than 0.5 mm/s for Sun-Probe-Earth (SPE) angles exceeding 40°.

Two-way Doppler relies on coherent repetition of a signal by an onboard transponder and circumvents frequency drift problems associated with onboard oscillators. Because one-way Doppler tracking is less accurate than two-way Doppler tracking, and because it represents a small fraction (<6%) of the entire data, we did not include one-way data in our analysis. Three-way data were not used in the analysis.

MESSENGER communications with Earth relied on the Deep Space Network (DSN) stations located in Goldstone (California), Madrid (Spain), and Canberra (Australia) and eight nonsteerable antennas mounted on the spacecraft. Two phased-array high-gain antennas (hereafter PAAs) provided the highest quality link. Two fanbeam antennas collocated with the PAAs provided a medium-gain link. The spacecraft was also equipped with four low-gain antennas (LGAs) [*Srinivasan et al.*, 2007]. MESSENGER operations relied on various combinations of these antennas depending on orbital geometry, spacecraft attitude, time of day, and scheduling constraints.

Earth-based antenna locations are known with an accuracy of centimeters in the 1993 realization of the International Earth Rotation Service Terrestrial Reference Frame [*Folkner*, 1997; *NASA Deep Space Network (DSN)*, 2014]. Spacecraft antenna coordinates are available in PDS documents [*Planetary Data System*, 2016b] and listed with five digits in Table 1. We applied the 0.89662 m correction to the spacecraft antenna coordinates [*Planetary Data System*, 2016b].

Tracking of the MESSENGER spacecraft by Earth-based antennas was not continuous. During the first (14 January 2008) and third (29 September 2009) flybys of Mercury, MESSENGER was occulted by Mercury immediately before and after the closest approach, respectively. No radio link was possible during the occultation periods. MESSENGER was tracked continuously during the second Mercury flyby (6 October 2008). During the orbital phase of the mission, MESSENGER was tracked for about 8 h/d, except in the first couple of weeks of orbital operations where it was tracked for about 16 h/d. After the 2012 mission extension, when MESSENGER's orbital period was reduced from 12 h to 8 h, MESSENGER was tracked for about 6 h/d.

3. Force and Measurement Models

We used the Mission Operations and Navigation Toolkit Environment (MONTE) software [*Evans et al.*, 2016] for orbit determination and parameter estimation. MONTE is developed and maintained by NASA's Jet Propulsion Laboratory (JPL). MONTE allows for precision modeling of the forces that act on the spacecraft and of the observables.

MONTE numerically integrates the equations of motion and computes partial derivatives with respect to the solve-for parameters. The MONTE integrator uses a variable-order Adams method for solving ordinary differential equations and is well suited for integrating trajectories.

A MONTE filter minimizes the residuals by adjusting the solve-for parameters and computes parameter uncertainties. The process relies on a *UD* Kalman filter [*Bierman*, 1977], where *U* is an upper triangular matrix with the diagonal elements equal to one and *D* is a diagonal matrix.

3.1. Gravitational Force Modeling

MONTE's representation of the gravity field follows the traditional spherical harmonic expansion of the potential [e.g., *Kaula*, 2000]:

$$U = \frac{GM}{r} + \frac{GM}{r}\sum_{l=2}^{\infty}\sum_{m=0}^{l}\left(\frac{R}{r}\right)^{l}\bar{P}_{l,m}(\sin\phi)\left(\bar{C}_{l,m}\cos(m\lambda) + \bar{S}_{l,m}\sin(m\lambda)\right), \quad (1)$$

where G is the gravitational constant, M is the mass of Mercury, $\bar{P}_{l,m}$ are the normalized associated Legendre polynomials of degree l and order m, R is the reference radius of Mercury (2440 km), and λ, ϕ, and r are the planetocentric longitude, latitude, and distance of MESSENGER from the origin of the reference frame, which is chosen to coincide with Mercury's center of mass. $\bar{C}_{l,m}$ and $\bar{S}_{l,m}$ are the normalized dimensionless spherical harmonic coefficients. We used the full normalization as described in *Kaula* [2000, p.7].

In addition to Mercury's gravitational forces, other gravitational forces included in our force budget are relativistic perturbations; gravitational perturbations from the Sun, Earth, and other planets computed from the DE432 [*Folkner*, 2014] planetary ephemerides; and perturbations due to solid tides raised on Mercury by the Sun.

We used the Earth-based radar solution [*Margot et al.*, 2012] as an priori estimate of Mercury's spin axis orientation, and we used the International Astronomical Union (IAU) value of the mean resonant spin rate [*Archinal et al.*, 2011]. Our libration model is based on the formulation of *Margot* [2009], where all amplitude coefficients have been scaled by a factor of 1.074 to account for improved estimates of the libration amplitudes between the initial [*Margot et al.*, 2007] and more recent [*Margot et al.*, 2012] estimates.

3.2. Nongravitational Force Modeling

The main nongravitational perturbations that affect MESSENGER's trajectory are solar radiation pressure, sunlight reflected by Mercury, thermal radiation emitted by Mercury, and propulsive maneuvers.

We used an eleven-element box model [*Vaughan et al.*, 2002] to compute radiative forces on the MESSENGER spacecraft. In this model, one cylindrical element represents the spacecraft bus, eight flat plates represent the spacecraft sunshade, and two flat plates represent the two solar panels. The contribution of each individual element to the spacecraft acceleration was computed on the basis of surface area, specular and diffuse reflectivity parameters, and the element's orientation in the body-fixed frame of the spacecraft. The orientation of the spacecraft bus and of the articulated solar panels can be obtained from quaternions defined in attitude data kernels provided by the MESSENGER team [*Planetary Data System*, 2016c].

The contributions of individual elements were then summed vectorially to obtain the total nongravitational acceleration due to the Sun (direct solar radiation) and Mercury (albedo and thermal emissivity). We assumed a uniform albedo distribution (0.074) and surface temperature for Mercury. The magnitude of the radiation pressure due to Mercury is an order of magnitude smaller than the solar radiation pressure. Accurate modeling of radiation pressure forces depends on the physical properties of the spacecraft box model, which are not perfectly known. In order to account for the inevitable mismodeling of these forces, we adjusted parameters representing the area of the model elements, the specular and diffusive reflectivity coefficients, and three scale factors (section 4.3). This approach takes care of modeling errors and is robust against the details of the spacecraft box model.

3.3. Measurement Modeling

Two-way radiometric measurements encode the propagation of the radio signal from the Earth-based antenna to the spacecraft antenna, coherent turnaround of the signal, and propagation back to the ground station. We extracted the observables (range and Doppler) from the Tracking and Navigation Files [*Planetary Data System*, 2016a] according to specifications of the TRK-2-34 format [*Soldan*, 2008]. We compressed the Doppler data by using an integration time of 30 s. Over the course of 30 s, the spacecraft traveled distances of at most ~120 km, which is less than the resolution of our expansion of the gravity field to degree and order 40.

We applied media corrections to the raw radiometric data to correct for the effects of the Earth's troposphere [*Planetary Data System*, 2016d] and ionosphere [*Planetary Data System*, 2016e]. Our tropospheric refraction delay model [*Moyer*, 2003; *Estefan and Sovers*, 1994] is composed of wet and dry mapping functions and their respective wet and dry zenith delays [*Niell*, 1996]. We used meteorological data [*Planetary Data System*, 2016f] collected at each DSN sites to compute these propagation delays.

Modeling of the DSN station positions included the effects of Earth's precession and nutation, Earth's polar motion, solid Earth tides, ocean loading, and tectonic plate motion [*NASA DSN*, 2014]. The positions of the spacecraft antennas with respect to MESSENGER's center of mass (Table 1) were held fixed.

Our processing of the Doppler and range data used the formulations by *Moyer* [2003] which are implemented in MONTE. Our propagation model includes a spacecraft transponder delay of 1379 ns [*Srinivasan et al.*, 2007].

4. Solution Technique

Our objectives were to obtain an independent solution for Mercury's gravity field, spin axis orientation, and Love number k_2. In this section we describe our procedures for determining the orbit of MESSENGER and for retrieving the geophysical parameters of Mercury.

4.1. Data Extent

We analyzed MESSENGER tracking data from the Mercury flybys that provided good radio science coverage (flybys 1 and 2). We also analyzed over 3 years of data from the orbital phase of the mission, from March 2011 to April 2014. With our integration time of 30 s, this data set contains about 780,000 Doppler points and 35,000 range points. The flyby data are important because the spacecraft was following a roughly east-west trajectory over the equator at the times of closest approach to the planet (~200 km above the surface), whereas the spacecraft followed a roughly north-south trajectory and remained at higher altitudes when crossing the equator (>1000 km above the surface) after orbit insertion.

We divided the radiometric data from the orbital phase into 2963 arcs, where each arc represents a continuous span of time corresponding to MESSENGER's orbital period. We selected the beginning of each arc to correspond to MESSENGER's apoapsis, i.e., the time when MESSENGER reached its farthest distance from Mercury. For the two flyby arcs that we processed, we selected the arc length corresponding to the interval during which MESSENGER was flying within Mercury's sphere of influence [*Danby*, 2003, pp. 352–353], approximately 10 and 11 h, respectively.

Several hundred arcs contained no radio science data at all because arc lengths are 8 to 12 h and DSN tracking typically lasted 6 to 8 h per day. Empty arcs were discarded.

We eliminated 914 arcs with Sun-Probe-Earth (SPE) angles below <40°. These arcs occur near superior solar conjunctions, where strong turbulent and ionized gases within the solar corona severely degrade the radio wave signal [*Asmar et al.*, 2005]. This degradation causes phase delays in the signal which are directly proportional to the total electron density and inversely proportional to the square of carrier radio wave frequency [*Asmar et al.*, 2005; *Verma et al.*, 2013].

We also excluded 141 arcs that were affected by spacecraft maneuvers, including momentum dump maneuvers and orbit correction maneuvers. Doing so allowed us to avoid errors due to strong unmodeled or mismodeled accelerations.

Finally, we excluded 4 arcs for which attitude information was incomplete and 9 arcs for which inspection of the pattern of residuals revealed obvious problems in data collection or quality. Among the remaining arcs, we excluded a number of outliers, i.e., individual data points that had unusually large residuals compared to simulated observables computed on the basis of a reference trajectory (Doppler residuals in excess of 100 mHz

and range residuals in excess of 1000 m). For this step, we used the trajectory produced by the navigation team, which was expedient but not required. The same outlier rejection step could have been performed with our own reconstructed trajectory, albeit with some additional processing. The fraction of outliers was about 3.1% of all tracking data. After this process of elimination, 1311 arcs remained.

4.2. Batch Processing

We distributed all 1311 arcs into 10 batches according to a simple prescription: batch i ($0 \leq i \leq 9$) contains all arcs with an arc number ending in i. The number of arcs per batch ranges from 124 to 135. This distribution resulted in a roughly uniform sampling of the geometrical circumstances and provided thorough longitudinal coverage in each batch.

The computational cost of the MONTE filter scales roughly as N^2M, where N is the number of solve-for parameters and M is the number of data points. Splitting the arcs into 10 separate batches enabled processing in parallel (one batch per computing node) and reduced the computational time by about an order of magnitude. This reduction in computational cost is the primary advantage of this batch processing technique.

In the weighted least squares estimation technique used in many geodesy applications, the entire data set is traditionally processed as a single batch [e.g., *Tapley et al.*, 2004; *Montenbruck and Gill*, 2012]. Our approach involves distributing the data in 10 separate batches. A potential disadvantage of splitting the data into batches as opposed to inverting all the data at once is that one or more batches could yield anomalous parameter solutions. We verified that there is excellent consistency across the 10 batch solutions by computing the corresponding standard deviations (sections 5.3 and 5.4). Another potential disadvantage of using multiple batches is that the traditional covariance matrix cannot be readily obtained. However, it is possible to approximate this matrix by taking the average of the covariance matrices obtained in each one of the 10 batches.

4.3. Solve-For Parameters

We used MONTE's filter module to refine estimates of solve-for parameters and their formal uncertainties. We grouped the estimated parameters into three categories: *arc level*, *batch level*, and *global*.

Arc-level parameters are those parameters that affect the measurements within a single arc. They consist of the spacecraft state vector (six parameters) at the initial epoch of each arc and of three scale factors to account for the mismodeling of accelerations due to solar radiation pressure, sunlight reflected by Mercury, and thermal emission from Mercury. The number of arc-level parameters is therefore equal to 9 times the number of arcs processed.

Batch-level parameters are those parameters that affect the measurements across multiple arcs. They consist of the *GM* of Mercury, 1677 coefficients for a spherical harmonic expansion to degree 40, the tidal Love number k_2, two angles specifying the spin axis orientation of Mercury, three parameters specifying the position of the spacecraft center of mass with respect to the spacecraft reference frame, three parameters for each one of the 11 elements of the spacecraft box model (surface area, specular reflectivity coefficient, and diffuse reflectivity coefficient), and Doppler and range biases for each one of the 12 ground-based antennas. Doppler and range biases are designed to absorb small errors in the knowledge of antenna positions or other undetected systematic effects. The Doppler biases (<3 mHz) are smaller than the RMS values of the residuals (section 5.2). The range biases capture any bias in the knowledge of the Earth-Mercury distance (section 5.5). The total number of batch-level parameters is 1741.

Global parameters are a subset of batch-level parameters that have geophysical significance. They consist of the *GM* of Mercury, spherical harmonics coefficients, the tidal Love number k_2, and two angles specifying the spin axis orientation of Mercury. Global parameters were calculated by taking the weighted mean of the independent estimates obtained from the 10 batches (section 4.4).

4.4. Solution Strategy

Our strategy consisted of three successive steps: numerical integration of the spacecraft state and its partial derivatives with respect to solve-for parameters, computation of range and Doppler values and their partial derivatives with respect to solve-for parameters at the epochs corresponding to the observables, and optimization of the arc-level and batch-level parameters to minimize the residuals between observed and computed values.

Figure 1 illustrates our solution strategy. Batch i ($1 \leq i \leq 10$) includes n_i data arcs.

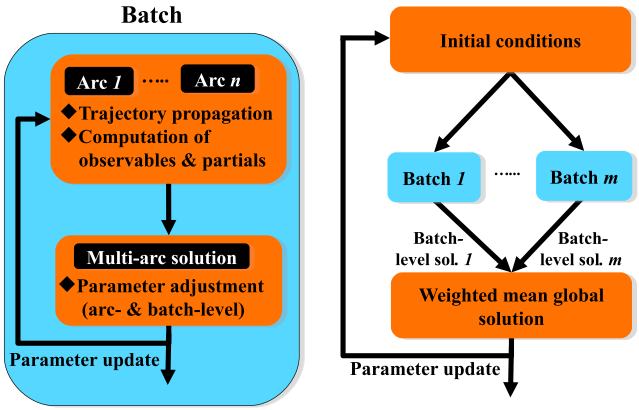

Figure 1. Orbit solution strategy.

As an expedient but optional step, we assigned the position and velocity of MESSENGER from the navigation solution [*Planetary Data System*, 2016g] as the initial state vector at the start of each arc. We performed separate orbit integrations for each arc and did not attempt to link integrations from consecutive arcs. An alternate choice would have been to use the state vector at the end of one arc to initiate the orbit integration for the next arc.

After integration of the orbit with the current values of the arc-level and batch-level solve-for parameters, we used our observation model (section 3.3) to compute range and Doppler values at the epochs corresponding to the observables. We computed the root-mean-square (RMS) values of the prefit residuals as

$$\mathrm{RMS}_j = \sqrt{\frac{1}{m_j}\sum_{k=1}^{m_j}(O_k - C_k)^2}, \tag{2}$$

where m_j is the number of data points in arc j ($1 \le j \le n_i$), O_k is the kth observable, and C_k is the corresponding computed value. We used the RMS values as an indication of the data quality in each arc and assigned observational uncertainties corresponding to RMS_j to each data point in arc j. Because most of the low-altitude data were acquired with the LGAs and because these data provide the best leverage on the recovery of the gravity field, we found that it was more effective to assign uniform uncertainties than to assign uncertainties on the basis of antenna gain.

Once the computed observables were generated for all arcs in a batch, we used MONTE's optimization filter (section 3) to simultaneously adjust arc-level and batch-level parameters. This optimization was informed by a priori uncertainties for some of the parameters (section 5). For the spin axis orientation and k_2 Love number, we used a bounded (± 3 times a priori uncertainty) optimization technique during the first iteration to rule out implausible values. The batch-level adjustments to the parameters is an iterative process resulting in new integrations with the updated parameter values (Figure 1, left). We stopped iterating when the change in the RMS value of the postfit residuals for the entire batch

$$\mathrm{RMS}_i = \sqrt{\frac{1}{n_i}\frac{1}{m_j}\sum_{j=1}^{n_i}\sum_{k=1}^{m_j}(O_k - C_k)^2}, \tag{3}$$

decreased by less than 10% compared to the previous iteration. Because batch-level estimates are further combined and used in a global iterative process with 10 iterations, we found that it was not worthwhile to decrease the batch-level stopping criterion below 10%.

Each batch provided an independent estimate of each one of the global solve-for parameters. To combine these estimates, we used a weighted mean technique in which a parameter estimate and its variance are given by

$$p = \frac{\sum_{i=1}^{10} w_i p_i}{\sum_{i=1}^{10} w_i} \tag{4}$$

$$\sigma_p^2 = \frac{1}{\sum_{i=1}^{10} w_i} \tag{5}$$

where $w_i = 1/\sigma_{p,i}^2$ is the weight corresponding to batch i and $\sigma_{p,i}$ is the formal uncertainty associated with parameter p and batch i.

Table 2. Comparison of Flyby Data Solutions HgMUCLA4x4 (This Work) and HGM001 [*Smith et al.*, 2010], With Formal Uncertainties of the Fit

Parameter	HgMUCLA4x4	HgM001
GM ($km^3\ s^{-2}$)	22031.88 ± 0.19	22031.80 ± 0.08
$\bar{C}_{2,0}$ (10^{-5})	-0.171 ± 0.5	-0.857 ± 1.8
$\bar{C}_{2,2}$ (10^{-5})	1.252 ± 0.7	1.258 ± 0.7

We used the weighted mean estimates and their uncertainties to update the dynamical model and iterated the entire process (Figure 1, right). Arc-level and nonglobal parameters were reset to their nominal values. After 10 iterations, the high-order gravity coefficients had an error spectrum that stabilized near the Kaula constraint (section 5.2) and other parameters exhibited variations that did not exceed the formal uncertainties of the fit.

5. Model Estimation

Our model estimation consisted of two major steps: analysis of flyby data (section 5.1) followed by estimation of a gravity field to degree and order 40 on the basis of both flyby and orbital data (section 5.2). We discuss separately our estimate of the tidal Love number k_2 (section 5.3), spin axis orientation (section 5.4), and Earth-Mercury distance error (section 5.5).

5.1. Flyby Analysis

We were interested in validating our ability to recover certain gravity quantities using only flyby data, and therefore, we first analyzed MESSENGER flyby data as if no orbital data existed.

During the first and third flybys, Mercury occulted MESSENGER, preventing radio frequency transmission near closest approach. Moreover, MESSENGER went into safe mode just before its closest approach to Mercury on the third flyby, resulting in the loss of tracking data. For these reasons, we did not include the third flyby in our analysis.

In our first estimation, we concentrated on the values of GM, $\bar{C}_{2,0}$, and $\bar{C}_{2,2}$. We used the Mariner 10 estimates of these quantities [*Anderson et al.*, 1987] as a priori estimates for this initial flyby solution. Other gravity coefficients were held fixed at zero. We verified that our procedures converged on the correct GM and $\bar{C}_{2,2}$ values even if we provided a priori information that differed markedly from the Mariner 10 values (e.g., $GM = 1000\ km^3\ s^{-2}$ and $\bar{C}_{2,2} = 0$). After this initial step, we used our estimates of GM, $\bar{C}_{2,0}$, and $\bar{C}_{2,2}$ as a priori estimates for a gravity solution to degree and order 4.

Our second estimation consisted of a gravity solution to degree and order 4 (HgMUCLA4x4). There was not sufficient coverage to expect a reliable recovery of $\bar{C}_{2,1}$ and $\bar{S}_{2,1}$, so these coefficients were held fixed at zero. All the gravity coefficients from this solution are within error bars of the coefficients obtained in the HgM001 flyby analysis of *Smith et al.* [2010]. Table 2 shows the most important values extracted from the HgMUCLA4x4 and HgM001 solutions.

The equatorial geometry of the MESSENGER flybys provided good sensitivity to the dynamical equatorial flattening $\bar{C}_{2,2}$ but poor sensitivity to the dynamical polar flattening $\bar{C}_{2,0}$. We therefore regard our initial estimate of $\bar{C}_{2,0}$ as unreliable, as did *Smith et al.* [2010]. Nevertheless, the GM and $\bar{C}_{2,2}$ values are both fully consistent with the analysis of orbital data. We used the HgMUCLA4x4 estimates of GM, $\bar{C}_{2,0}$, and $\bar{C}_{2,2}$ as a priori estimates for a gravity solution to degree and order 40.

5.2. Gravity Field Solution HgMUCLA40x40

The gravity field solution that we obtained from more than 3 years of MESSENGER tracking data, hereafter HgMUCLA40x40, produces very good measurement residuals (Figure 2). The RMS values of the residuals are better than the instrument measurement requirement (~0.1 mm/s or ~5.6 mHz [*Srinivasan et al.*, 2007]) and give confidence about the quality of the fit and the recovery of estimated parameters.

The power associated with degree l in a spherical harmonic expansion is given by

$$P_l = \sqrt{\frac{1}{(2l+1)} \sum_{m=0}^{l} \left(\bar{C}_{l,m}^2 + \bar{S}_{l,m}^2 \right)}. \tag{6}$$

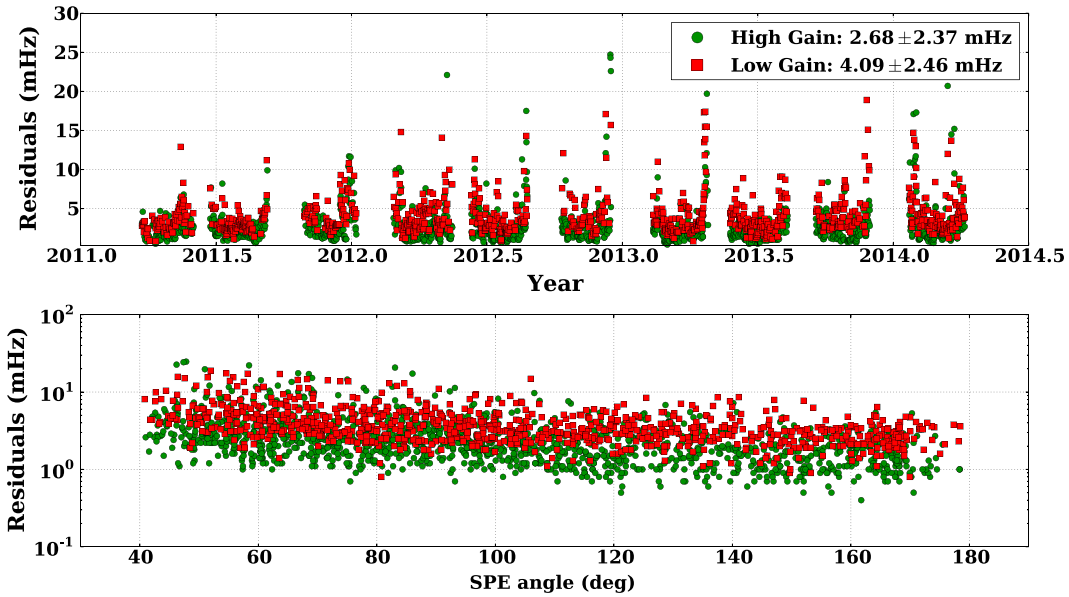

Figure 2. RMS values of two-way Doppler residuals obtained after fitting arc-level parameters for each data arc using the HgMUCLA40x40 gravity field solution, shown as a (top) function of time and (bottom) SPE angle. The visible gaps between clusters of points correspond to periods of superior conjunction (SPE $\leq$ 40°), which we excluded from the analysis (section 4.1). Each point in the figure represents the RMS value of residuals for individual arcs as computed by equation (2). Residuals associated with high-gain antennas are generally lower than those associated with low-gain antennas, as expected. Values in the rectangular box represent the mean and standard deviation of the residuals calculated over the entire data set.

The power associated with HgMUCLA40x40 harmonics of degree l compares favorably with that of other solutions (Figure 3). In order to limit the power at high degrees in our solution to degree and order 40, we placed a priori constraints on the uncertainties associated with each coefficient of degree l ($7 \leq l \leq 40$) equal to K/l^2. This is the well-know Kaula constraint. We experimented with a few values of K and settled on the value adopted by *Mazarico et al.* [2014], $K = 1.25 \times 10^{-5}$. Application of a Kaula constraint helped mitigate against spurious results due to the lack of low-altitude coverage in the Southern Hemisphere, such as the development of large gravity anomalies. As a test, we obtained a gravity solution to degree and order 15 without applying the Kaula constraint to verify that this constraint is necessary for degrees $l > 6$ (Figure 3).

The HgMUCLA40x40 values of GM and low-degree coefficients (Table 3) are in excellent agreement with the HgM005 solution of *Mazarico et al.* [2014]. The low-degree coefficients play a vital role in understanding the planet's interior structure [e.g., *Margot et al.*, 2012]. In particular, the second-degree coefficients $C_{2,0}$ and $C_{2,2}$, combined with spin state parameters, can be used to estimate the moment of inertia of the planet and that of its core. We find that $C_{2,0} = -5.033 \times 10^{-5}$ and $C_{2,2} = 8.067 \times 10^{-6}$ are within 0.05% and 0.3% of the *Smith et al.* [2012] values that have been used to infer properties of Mercury's interior [*Margot et al.*, 2012; *Hauck et al.*, 2013; *Rivoldini and Van Hoolst*, 2013], adding confidence to these studies. Mercury's oblateness $J_2 = -C_{2,0}$.

Our estimates of other degree-2 coefficients, $C_{2,1}$, $S_{2,1}$, and $S_{2,2}$, are not consistent with those of *Mazarico et al.* [2014] if we use error bars corresponding to the formal uncertainties of the fit. However, the values are consistent if these formal uncertainties are multiplied by a factor of 10–15 to arrive at more realistic error bars, as suggested by *Mazarico et al.* [2014] and other geodetic studies. The difficulty in reliably estimating these coefficients can be explained in part by the fact that they are 3–4 orders of magnitude smaller than $C_{2,2}$. If Mercury were a principal axis rotator and if we had perfect knowledge of its orientation, we would expect $C_{2,1} = S_{2,1} = S_{2,2} = 0$. Our values are close to zero (Table 3). The misalignment between Mercury's long axis and that prescribed by the orientation model of *Margot* [2009] is only $\delta\phi = 1/2\text{atan}(S_{2,2}/C_{2,2}) = 0.019°$, suggesting that both the orientation model and the recovery of $S_{2,2}$ are satisfactory. Our estimate of $\delta\phi$ has a magnitude that is about 40% of the value of *Mazarico et al.* [2014] and the opposite sign. In contrast, the IAU-defined prime meridian differs by about 0.2° (~8 km) from the geophysically relevant origin of longitude, i.e., the longitude that is defined by the principal axes of inertia and that faces the Sun at every other perihelion passage.

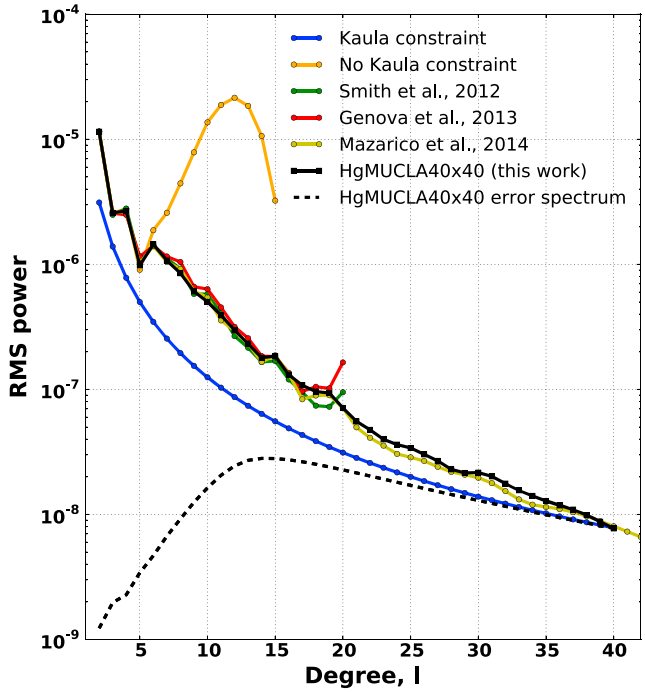

Figure 3. Power associated with degree l in several spherical harmonic expansions of the gravity field. HgMUCLA40x40 (this work) is shown with the solid black line. The solid blue line illustrates the a priori Kaula constraint that was used for degrees $l > 6$. The dashed black line illustrates the error spectrum. The magnitude of the formal uncertainties associated with our analysis approaches the magnitude of the coefficients at degree $l \sim 40$, where the solid and dashed black lines intersect. The solid orange line depicts the power spectrum obtained when the Kaula constraint is not applied.

A spherical harmonic expansion of the shape of Mercury reveals a long axis that is offset by 15° [*Perry et al.*, 2015] compared to the principal axis of inertia defined here.

Other zonal coefficients have a special significance in the context of mission planning. Knowledge of $C_{3,0}$ and $C_{4,0}$ can help predict the evolution of the orbit of BepiColombo, a planned spacecraft mission to Mercury [*Genova et al.*, 2013]. Our estimates of $C_{3,0}$ and $C_{4,0}$ agree within 1.1% and 0.7% of the HgM005 values, respectively.

Table 3 shows that our estimate of GM is also fully consistent with the HgM005 value. The agreement between two independent solutions gives confidence in the robustness of the force and data models as well as in the

Table 3. Select Coefficients of HgMUCLA40x40 Solution (This Work) Compared With Those of the HgM005 Solution [*Mazarico et al.*, 2014], Showing the Fractional Change Δ Between the Solutions[a]

	HgMUCLA40x40		HgM005		
Parameter	Value	Formal Uncertainty	Value	Formal Uncertainty	Δ
GM (km^3s^{-2})	22031.87404	9×10^{-5}	22031.87080	9×10^{-5}	-1.5×10^{-7}
$\bar{C}_{2,0}$	-2.25100×10^{-5}	1.3×10^{-9}	-2.25045×10^{-5}	0.7×10^{-9}	-2.5×10^{-4}
$\bar{C}_{2,1}$	-9.11665×10^{-9}	1.1×10^{-9}	-1.61526×10^{-8}	0.4×10^{-9}	4.4×10^{-1}
$\bar{S}_{2,1}$	5.63022×10^{-9}	1.1×10^{-9}	-1.36488×10^{-8}	0.4×10^{-9}	$1.4 \times 10^{+0}$
$\bar{C}_{2,2}$	1.24973×10^{-5}	1.2×10^{-9}	1.24538×10^{-5}	0.4×10^{-9}	-3.5×10^{-3}
$\bar{S}_{2,2}$	8.52067×10^{-9}	1.3×10^{-9}	-2.09078×10^{-8}	2.2×10^{-9}	$1.4 \times 10^{+0}$
$\bar{C}_{3,0}$	-4.71444×10^{-6}	1.6×10^{-9}	-4.76589×10^{-6}	1.6×10^{-9}	1.1×10^{-2}
$\bar{C}_{4,0}$	-5.89291×10^{-6}	2.4×10^{-9}	-5.84911×10^{-6}	4.7×10^{-9}	-7.5×10^{-3}
$\bar{C}_{5,0}$	2.98686×10^{-7}	3.5×10^{-9}	2.79497×10^{-7}	1.2×10^{-8}	-6.9×10^{-2}
$\bar{C}_{6,0}$	1.90218×10^{-6}	5.1×10^{-9}	1.45853×10^{-6}	2.6×10^{-8}	1.5×10^{-2}

[a]Our adopted error bars are 10 times the formal uncertainties listed.

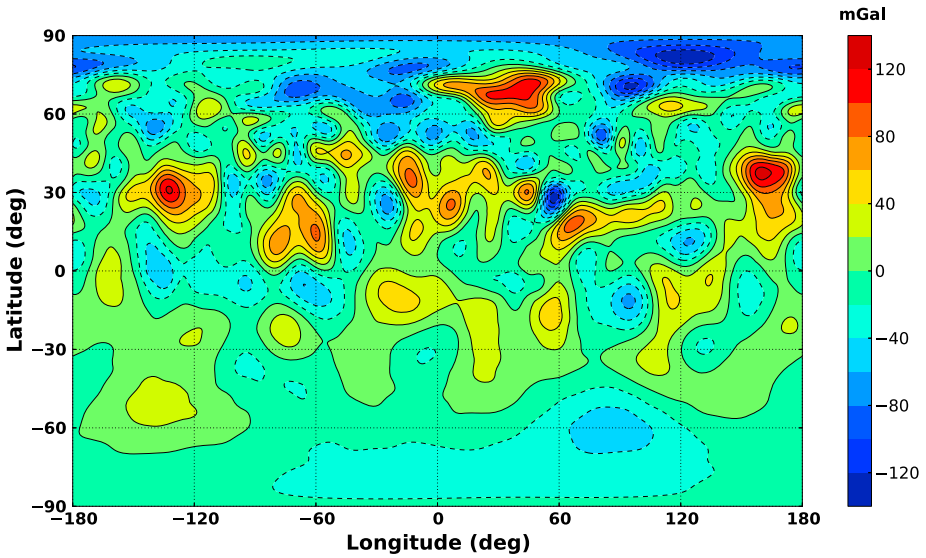

Figure 4. Free-air gravity anomalies (mGal) shown on a cylindrical projection. A mGal corresponds to 10^{-5}ms^{-2}, which is ~1 ppm and ~3 ppm of the acceleration at the surface of Earth and Mercury, respectively. A large positive gravity anomaly is observed within the Caloris Basin plains near 160° E. longitude, 37° latitude.

overall solution strategies. HgMUCLA40x40 and HgM005 were obtained with different software and different approaches. Neither solution relied on a priori information other than the Mariner 10 results [*Anderson et al.*, 1987].

Our gravity field solution enables the calculation of free-air gravity anomalies, which are useful in detecting internal density inhomogeneities and in evaluating the degree of isostatic adjustment of geological features. Our map of free-air gravity anomalies (Figure 4) is similar to the map derived from HgM005. Expansions of the geoid or free-air gravity anomalies can be used to compute gravity-to-topography admittance ratios and evaluate the thickness of Mercury's crust [e.g., *Padovan et al.*, 2015; *James et al.*, 2015].

5.3. Tidal Love Number k_2

A measurement of the tidal Love number k_2 is useful because it enables us to rule out a range of interior models that are otherwise compatible with observations of the spin and gravity of Mercury. The Love number can also inform us about the mechanical properties of the mantle and the possibility of a solid FeS layer at the top of the core [*Padovan et al.*, 2014].

We obtained an independent estimate of the tidal Love number k_2 as part of our gravity solution HgMUCLA40x40. We used the 0.485 ± 0.035 mean value of the theoretical estimates [*Padovan et al.*, 2014] as an a priori value and uncertainty. Our solution is

$$k_2 = 0.464 \pm 0.023, \tag{7}$$

where the adopted error bar corresponds to 10 times the formal uncertainty of the fit. The standard deviation of the k_2 estimates across the 10 individual batch solutions is 0.0041, a factor of ~5 smaller than our adopted uncertainty. We also solved for k_2 with different initial conditions. In a first test, we repeated our procedure with a variety of initial conditions ($k_2 = 0.42, 0.45, 0.51$) and found results consistent with our adopted solution. In a second test, we started with extreme values ($k_2 = 0$ and $k_2 = 1$) and a large a priori uncertainty ($\sigma_{k_2} = 0.5$) in the simpler case of a gravity field with degree and order 20. We found $k_2 = 0.42 \pm 0.04$ in both instances, suggesting that we arrive at roughly the same k_2 value regardless of starting condition. Our preferred value is the HgMUCLA40x40 solution (equation (7)), which is compatible with the value of *Mazarico et al.* [2014] and the computed value of *Padovan et al.* [2014]. We emphasize that a reliable measurement of k_2 from MESSENGER tracking data is challenging because the spacecraft is in a highly eccentric orbit and is also subject to substantial nongravitational perturbations. In the course of our gravity solutions with different strategies and parameters, we encountered best fit values for k_2 in the range 0.420–0.465.

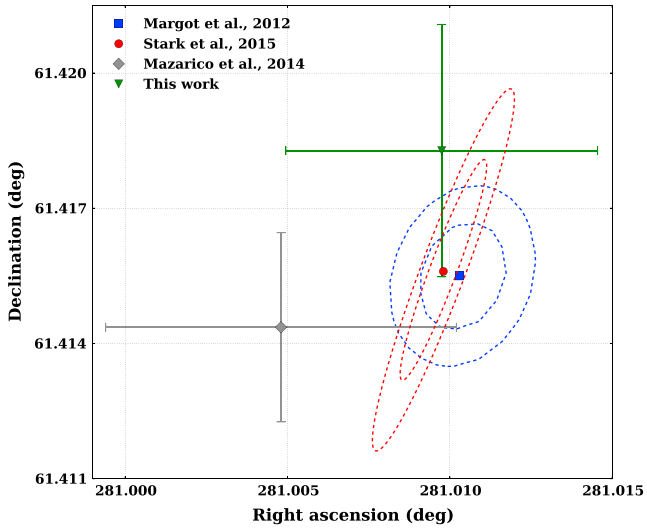

Figure 5. Spin axis orientation solutions: Earth-based radar (blue), altimeter + DEMs (red), HgM005 gravity (gray), and HgMUCLA40x40 gravity (green, this work).

5.4. Spin Axis Orientation

A priori values for the spin state of Mercury were based on the libration model of *Margot* [2009] with small adjustments to the libration amplitude and spin orientation values as recommended by *Margot et al.* [2012] (section 3.1). Although we did not attempt to fit for the spin rate or libration amplitude at this time, our model can be expanded to perform such a fit in the future. To do so, we would express Mercury's rotational phase as a trigonometric series and solve for the series coefficients.

The recovery of the spin axis orientation exhibited good consistency across the 10 individual batch solutions. The standard deviations of the right ascension and declination estimates across the 10 batches are 0.00089° and 0.00063°, respectively. Our final, weighted mean estimate of the spin axis orientation at epoch J2000.0 is

$$\mathrm{RA} = 281.00975° \pm 0.0048°, \tag{8}$$

$$\mathrm{DEC} = 61.41828° \pm 0.0028°, \tag{9}$$

where we adopted error bars corresponding to 10 times the formal uncertainties of the fit. Our gravity-based estimate of the spin axis orientation is within 10 arc sec of the independent crust-based estimates of *Margot et al.* [2012] and *Stark et al.* [2015] (Figure 5). The convergence of all three values is important because of the profound impact of Mercury's obliquity on the determination of the moment of inertia and, consequently, on the construction of accurate interior models. Our solution is 16 arc sec away from and only marginally consistent with the gravity-based estimate of *Mazarico et al.* [2014]. The lack of a better agreement between HgMUCLA40x40 and HgM005 for the spin pole parameters despite a generally excellent agreement in the gravity coefficients is worth noting. We speculate that the difference might be due to our use of an improved ephemeris, DE432, compared to *Mazarico et al.* [2014]'s use of DE423, or to our inclusion of range data, which they may not have included.

5.5. Earth-Mercury Distance Error

Range measurements to the MESSENGER spacecraft currently provide the best way of improving the knowledge of Mercury's position [*Verma et al.*, 2014; *Mazarico et al.*, 2014; *Fienga et al.*, 2015]. We used DE432 [*Folkner*, 2014] as the nominal planetary ephemeris when deriving the HgMUCLA40x40 gravity solution. We computed MESSENGER range residuals using this ephemeris and compared them to the residuals obtained with DE423 [*Folkner*, 2010], DE430 [*Folkner et al.*, 2014], and INPOP13c [*Fienga et al.*, 2015]. Figure 6 illustrates the remaining Earth-Mercury distance error in the various ephemeris versions. DE423 includes range data obtained during MESSENGER flybys but not during the orbital phase of the mission and retains errors in Earth-Mercury distance at the ~100 m level. DE430 includes range data from the first 6 months of the orbital phase. Both DE432 and INPOP13c include several years of range data from the orbital phase of the mission.

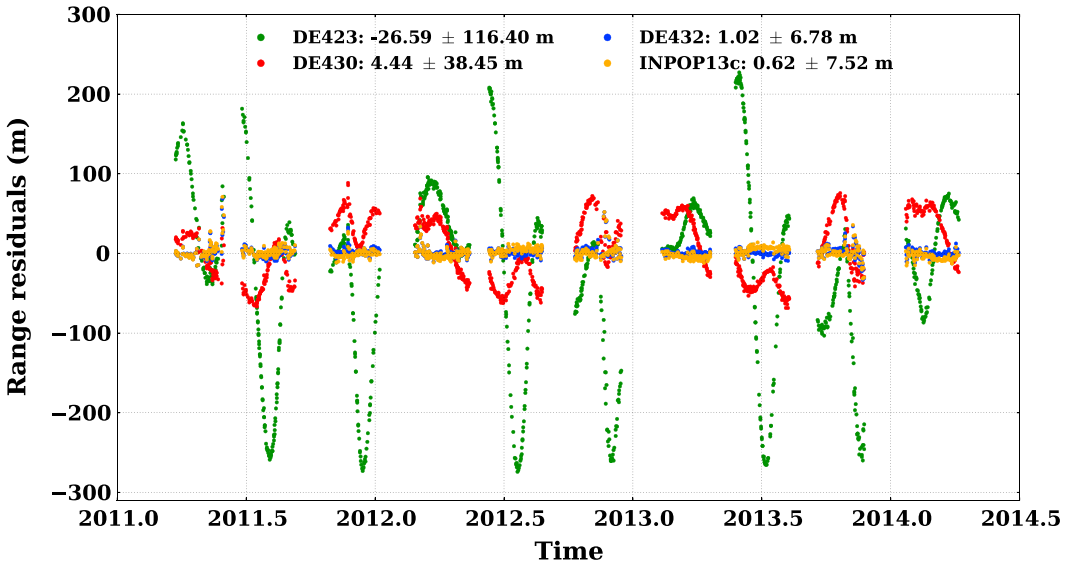

Figure 6. One-way range residuals obtained with the DE423, DE430, DE432, and INPOP13c planetary ephemerides. Each point represents the mean residual corresponding to an individual arc. The legend shows the mean and standard deviation of the residuals for each data set. Gaps correspond to solar conjunction periods (SPE < 40°).

Although the mean of INPOP13c residuals is lower than that of DE432 due to fortuitous cancellation of positive and negative values, close inspection reveals that systematic patterns in the residuals are more pronounced in the INPOP13c solution. Thanks to MESSENGER data, the knowledge of the Earth-Mercury distance in the 2011–2014 interval is now at the ~7 m level. MESSENGER range and Doppler data can be combined with similar data from other missions as well as radar and optical astrometry of all planets and asteroids to further improve solar system ephemerides.

6. Discussion

Our recovery of low-degree coefficients in the spherical harmonic expansion of the gravity field is generally in good agreement with previous results (Table 3).

The gravity-based solution of *Mazarico et al.* [2014] for Mercury's spin axis orientation was found to be marginally consistent with the Earth-based radar and topography-based solutions (Figure 5) but also sufficiently different to raise questions about the possibility of a discrepancy. A discrepancy would indicate either an error in one of the determinations or a real difference between the orientations about which the gravity field and the crust rotate. Although the latter prospect is intriguing, we find no convincing evidence for a discrepancy. Our spin pole estimate is close (10 arc sec) to the crust-based spin pole measurements but in a different direction than that identified by *Mazarico et al.* [2014]. The most plausible conclusion is that both gravity-based estimates are marginally consistent with the crust-based estimates and that the gravity field and crust rotate about nearly the same axis.

Our recovery of Mercury's spin axis orientation from gravity data alone suggests that gravity-based methods can be applied successfully to reach a similar goal at other bodies. Other examples include the gravity-based spin axis orientation of Venus [*Konopliv et al.*, 1999] which is on the edge of the uncertainty region of the crust-based estimate [*Davies et al.*, 1992]. The situation at Mars is not directly comparable due to the availability of data from multiple long-lived landers. The gravity-based spin axis orientation of Vesta [*Konopliv et al.*, 2014] is in good agreement with the crust-based estimate [*Russell et al.*, 2012].

Our estimate of Mercury's tidal Love number ($k_2 = 0.464 \pm 0.023$) is larger than an existing determination [$k_2 = 0.451 \pm 0.014$, *Mazarico et al.*, 2014] and admits a wider range of interior models. *Padovan et al.* [2014] simulated the tidal response of Mercury on the basis of tens of thousands of interior models with different physical properties. Two parameters that strongly influence the tidal response are the temperature at the base of the mantle and the rigidity of the mantle (Figure 7). *Padovan et al.* [2014] showed that the k_2 estimate of *Mazarico et al.* [2014] favors a cold and stiff mantle (basal temperature of 1600 K, rigidity of 71 GPa) with no

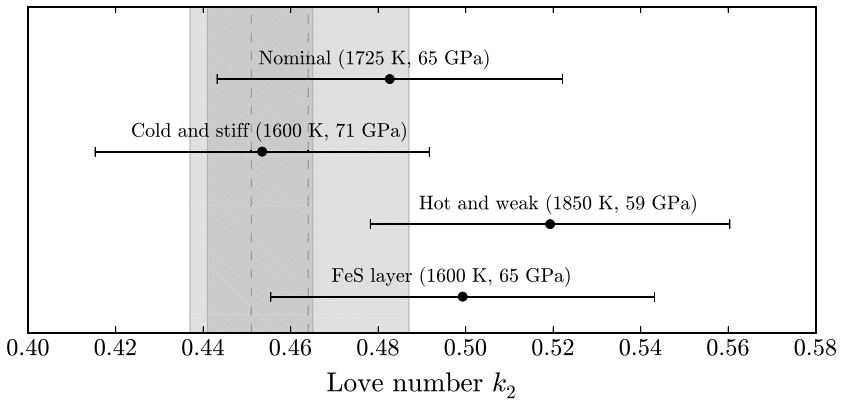

Figure 7. Comparison of measured and calculated values of the tidal Love number k_2. The black solid dots with error bars represent four classes of models investigated by *Padovan et al.* [2014] with different assumptions about the basal temperature and rigidity of the outer shell. The vertical dashed lines correspond to our measured k_2 value and that of *Mazarico et al.* [2014]. The descending hatch pattern represents the one standard deviation uncertainties of *Mazarico et al.* [2014]. Our adopted uncertainties are shown with the ascending hatch pattern.

FeS layer. Our Love number determination is compatible with a substantially larger set of models, including *Padovan et al.* [2014]'s nominal class of models with a hotter and weaker mantle (basal temperature of 1725 K, rigidity of 65 GPa). It is also compatible with models that include an FeS layer at the bottom of the mantle and even with a small fraction of hot and weak models (basal temperature of 1850 K, rigidity of 59 GPa).

7. Conclusions

We analyzed over 3 years of MESSENGER radio tracking data. We estimated parameters that describe a spherical harmonic expansion to degree and order 40 of Mercury's gravity field as well as the tidal Love number and spin axis orientation. Our solution for Mercury's mass and gravity field is in excellent agreement with previous estimates. In particular, recovery of the $C_{2,0}$ and $C_{2,2}$ coefficients gives additional confidence in prior inferences about Mercury's moment of inertia and interior structure. Our estimate of the tidal Love number is larger than *Mazarico et al.* [2014]'s estimate, which favored interior models with a cold and stiff mantle. Our estimate is compatible with a wider range of interior models, including models with a hotter and weaker mantle. Our spin state solution is consistent with previous measurements of the orientation of the crust but only marginally consistent with *Mazarico et al.* [2014]'s estimate. We hypothesize that the difference is related to our use of an improved ephemeris with range residuals at the ~7 m level (versus ~116 m) or to our inclusion of range data in the solution. Finally, we confirmed that the Earth-Mercury distance in the 2011–2014 interval is now known to be better than 10 m.

Acknowledgments
We thank anonymous reviewers for their suggestions that improved the manuscript. This work was enabled in part by the Mission Operations and Navigation Toolkit Environment (MONTE). MONTE is developed at the Jet Propulsion Laboratory, which is operated by Caltech under contract with NASA. The archive locations for the data used in this work are listed in the text and references. The HgMUCLA40x40 coefficient values and uncertainties are available from the University of California archive escholarship at http://escholarship.org/uc/item/74c8x8mj. A.K.V. and J.L.M. were supported in part by the NASA Planetary Astronomy program under grant NNX12AG34G and by the MESSENGER Participating Scientist program under grant NNX09AR45G.

References

Anderson, J. D., G. Colombo, P. B. Esposito, E. L. Lau, and G. B. Trager (1987), The mass, gravity field, and ephemeris of Mercury, *Icarus*, *71*, 337–349.
Archinal, B. A., et al. (2011), Report of the IAU working group on cartographic coordinates and rotational elements: 2009, *Celest. Mech. Dyn. Astron.*, *109*, 101–135.
Asmar, S. W., J. W. Armstrong, L. Iess, and P. Tortora (2005), Spacecraft Doppler tracking: Noise budget and accuracy achievable in precision radio science observations, *Radio Sci.*, *40*, RS2001, doi:10.1029/2004RS003101.
Bierman, G. J. (1977), *Factorization Methods for Discrete Sequential Estimation*, vol. 128, p. 241, Academic Press, New York.
Danby, J. M. A. (2003), *Fundamentals of Celestial Mechanics*, 2. ed., rev. and enlarged, 5. print. ed., pp. 352–353, Willman-Bell, Richmond, Va.
Davies, M. E., T. R. Colvin, P. G. Rogers, P. W. Chodas, W. L. Sjogren, E. L. Akim, V. A. Stepaniants, Z. P. Vlasova, and A. I. Zakharov (1992), The rotation period, direction of the north pole, and geodetic control network of Venus, *J. Geophys. Res.*, *97*, 13,141–13,151.
Estefan, J. A., and O. J. Sovers (1994), A comparative survey of current and proposed tropospheric refraction-delay models for DSN radio metric data calibration, *Tech. Rep., NASA-CR-197338, JPL-PUBL-94-24, NAS 1.26:197338*, Jet Propul. Lab., Pasadena, Calif.
Evans, S., W. Taber, T. Drain, J. Smith, H. C. Wu, M. Guevara, R. Sunseri, and J. Evans (2016), MONTE: The next generation of mission design and navigation software, in *The 6th International Conference on Astrodynamics Tools and Techniques (ICATT)*, International Conference on Astrodynamics Tools and Techniques, Darmstadt, Germany.
Fienga, A., H. Manche, J. Laskar, M. Gastineau, and A. Verma (2015), INPOP new release: INPOP13c, *ArXiv e-prints*.
Folkner, W. M. (1997), DSN station locations and uncertainties, *Tech. Rep.*, Jet Propul. Lab., Pasadena, Calif.
Folkner, W. M. (2010), Planetary ephemeris DE423 fit to Messenger encounters with Mercury, *Tech. Rep.*, Jet Propul. Lab., Pasadena, Calif.
Folkner, W. M. (2014), Planetary ephemeris DE432, *Tech. Rep.*, Jet Propul. Lab., Pasadena, Calif.
Folkner, W. M., J. G. Williams, D. H. Boggs, R. S. Park, and p. Kuchynka (2014), The planetary and lunar ephemerides DE430 and DE431, *Tech. Rep.*, Jet Propul. Lab., Pasadena, Calif.

Genova, A., L. Iess, and M. Marabucci (2013), Mercury's gravity field from the first six months of MESSENGER data, *Planet. Space Sci.*, *81*, 55–64, doi:10.1016/j.pss.2013.02.006.
Hauck, S. A., et al. (2013), The curious case of Mercury's internal structure, *J. Geophys. Res. Planets*, *118*, 1204–1220, doi:10.1002/jgre.20091.
James, P. B., M. T. Zuber, R. J. Phillips, and S. C. Solomon (2015), Support of long-wavelength topography on Mercury inferred from MESSENGER measurements of gravity and topography, *J. Geophys. Res. Planets*, *120*, 287–310, doi:10.1002/2014JE004713.
Kaula, W. M. (2000), *Theory of Satellite Geodesy: Applications of Satellites to Geodesy*, Dover Publ., Mineola, New York.
Konopliv, A. S., W. B. Banerdt, and W. L. Sjogren (1999), Venus gravity: 180th degree and order model, *Icarus*, *139*, 3–18.
Konopliv, A. S., et al. (2014), The Vesta gravity field, spin pole and rotation period, landmark positions, and ephemeris from the Dawn tracking and optical data, *Icarus*, *240*, 103–117.
Margot, J. L. (2009), A Mercury orientation model including non-zero obliquity and librations, *Celest. Mech. Dyn. Astron.*, *105*, 329–336.
Margot, J. L., S. J. Peale, R. F. Jurgens, M. A. Slade, and I. V. Holin (2007), Large longitude libration of Mercury reveals a molten core, *Science*, *316*, 710–714.
Margot, J. L., S. J. Peale, S. C. Solomon, S. A. Hauck II, F. D. Ghigo, R. F. Jurgens, M. Yseboodt, J. D. Giorgini, S. Padovan, and D. B. Campbell (2012), Mercury's moment of inertia from spin and gravity data, *J. Geophys. Res.*, *117*, E00L09, doi:10.1029/2012JE004161.
Mazarico, E., A. Genova, S. Goossens, F. G. Lemoine, G. A. Neumann, M. T. Zuber, D. E. Smith, and S. C. Solomon (2014), The gravity field, orientation, and ephemeris of Mercury from MESSENGER observations after three years in orbit, *J. Geophys. Res. Planets*, *119*, 2417–2436, doi:10.1002/2014JE004675.
Montenbruck, O., and E. Gill (2012), *Satellite Orbits: Models, Methods, and Applications*, Springer, Berlin.
Moyer, T. D. (2003), *Formulation for Observed and Computed Values of Deep Space Network Data Types for Navigation*, vol. 2, John Wiley, Hoboken, N. J.
NASA DSN (2014), DSN Telecommunications link design handbook, *(810-005, 301, Rev. J) Tech. Rep.*, Jet Propul. Lab., Pasadena, Calif.
Niell, A. E. (1996), Global mapping functions for the atmosphere delay at radio wavelengths, *J. Geophys. Res.*, *101*, 3227–3246, doi:10.1029/95JB03048.
Padovan, S., J. L. Margot, S. A. Hauck, B. Moore, and S. C. Solomon (2014), The tides of Mercury and possible implications for its interior structure, *J. Geophys. Res.*, *119*, 850–866, doi:10.1002/2013JE004459.
Padovan, S., M. A. Wieczorek, J. L. Margot, N. Tosi, and S. C. Solomon (2015), Thickness of the crust of Mercury from geoid-to-topography ratios, *Geophys. Res. Lett.*, *42*, 1029–1038, doi:10.1002/2014GL062487.
Peale, S. J., J.-L. Margot, S. A. Hauck, and S. C. Solomon (2016), Consequences of a solid inner core on Mercury's spin configuration, *Icarus*, *264*, 443–455.
Perry, M. (2011), MESSENGER Radio Science Raw Data Archive Experimental Data Records (EDR) Software Interface Specification (SIS), *Tech. Rep.*, Johns Hopkins Univ. Appl. Phys. Lab., (JHU/APL), Laurel, Md.
Perry, M. E., et al. (2015), The low-degree shape of Mercury, *Geophys. Res. Lett.*, *42*, 6951–6958, doi:10.1002/2015GL065101.
Planetary Data System (2016a), Radio tracking data. [Available at http://pds-geosciences.wustl.edu/messenger/mess-v_h-rss-1-edr-rawdata-v1/messrs_0xxx/data/tnf/, Accessed date 18 March 2016.]
Planetary Data System (2016b), Spacecraft antenna coordinates. [Available at http://naif.jpl.nasa.gov/pub/naif/pds/data/mess-e_v_h-spice-6-v1.0/messsp_1000/data/ik/msgr_rs_v111.ti/, Accessed date 18 March 2016.]
Planetary Data System (2016c), Attitude data. [Available at ftp://naif.jpl.nasa.gov/pub/naif/pds/data/mess-e_v_h-spice-6-v1.0/messsp_1000/data/ck/, Accessed date 18 March 2016.]
Planetary Data System (2016d), Earth troposphere. [Available http://pds-geosciences.wustl.edu/messenger/mess-v_h-rss-1-edr-rawdata-v1/messrs_0xxx/ancillary/tro/, Accessed date 18 March 2016.]
Planetary Data System (2016e), Earth ionosphere. [Available http://pds-geosciences.wustl.edu/messenger/mess-v_h-rss-1-edr-rawdata-v1/messrs_0xxx/ancillary/ion/, Accessed date 18 March 2016.]
Planetary Data System (2016f), Meteorological data. [Available at http://pds-geosciences.wustl.edu/messenger/mess-v_h-rss-1-edr-rawdata-v1/messrs_0xxx/ancillary/wea/, Accessed date 18 March 2016.]
Planetary Data System (2016g), Navigation trajectory data. [Available at ftp://naif.jpl.nasa.gov/pub/naif/pds/data/mess-e_v_h-spice-6-v1.0/messsp_1000/data/spk/, Accessed date 18 March 2016.]
Rivoldini, A., and T. Van Hoolst (2013), The interior structure of Mercury constrained by the low-degree gravity field and the rotation of Mercury, *Earth Planet. Sci. Lett.*, *377*, 62–72.
Russell, C. T., et al. (2012), Dawn at Vesta: Testing the protoplanetary paradigm, *Science*, *336*, 684.
Smith, D. E., et al. (2010), The equatorial shape and gravity field of Mercury from MESSENGER flybys 1 and 2, *Icarus*, *209*, 88–100.
Smith, D. E., et al. (2012), Gravity field and internal structure of Mercury from MESSENGER, *Science*, *336*, 214–217.
Soldan, H. (2008), DNS tracking system data archival format, *Tech. Rep.*, Deep Space Network External Interface Specification, JPL D-16765, 820-013, Jet Propul. Lab., Pasadena, Calif.
Solomon, S. C., et al. (2001), The MESSENGER mission to Mercury: Scientific objectives and implementation, *Planet. Space Sci.*, *49*, 1445–1465.
Srinivasan, D. K., M. E. Perry, K. B. Fielhauer, D. E. Smith, and M. T. Zuber (2007), The radio frequency subsystem and radio science on the MESSENGER mission, *Space Sci. Rev.*, *131*, 557–571, doi:10.1007/s11214-007-9270-7.
Stark, A., J. Oberst, F. Preusker, S. J. Peale, J. L. Margot, R. J. Phillips, G. A. Neumann, D. E. Smith, M. T. Zuber, and S. C. Solomon (2015), First MESSENGER orbital observations of Mercury's librations, *Geophys. Res. Lett.*, *42*, 7881–7889, doi:10.1002/2015GL065152.
Tapley, B., B. Schutz, and G. Born (2004), *Statistical Orbit Determination*, Elsevier Acad. Press, London, U. K.
Vaughan, R. M., D. R. Haley, H. S. Shapiro, and D. J. O'Shaughnessy (2002), Momentum management for the MESSENGER mission, *Adv. Astronaut. Sci.*, *109*, 1139–1158.
Verma, A. K., A. Fienga, J. Laskar, K. Issautier, H. Manche, and M. Gastineau (2013), Electron density distribution and solar plasma correction of radio signals using MGS, MEX, and VEX spacecraft navigation data and its application to planetary ephemerides, *Astron. Astrophys.*, *550*, A124, doi:10.1051/0004-6361/201219883.
Verma, A. K., A. Fienga, J. Laskar, H. Manche, and M. Gastineau (2014), Use of MESSENGER radioscience data to improve planetary ephemeris and to test general relativity, *Astron. Astrophys.*, *561*, A115, doi:10.1051/0004-6361/201322124.
Zuber, M. T., and D. E. Smith (1997), Remote sensing of planetary librations from gravity and topography data: Mercury simulation, *Lunar Planet. Sci.*, *28*, 1637–1638.